A Snowfall Detection Algorithm for ATMS Over Ocean, Sea Ice, and Coast

Yalei You [ID], Huan Meng, Jun Dong, Yongzhen Fan, Ralph R. Ferraro, Guojun Gu, and Likun Wang [ID]

Abstract—This study developed a snowfall detection algorithm over ocean, sea ice, and coast for the advanced technology microwave sounder (ATMS) onboard both NPP and NOAA-20 satellites. The detection algorithm was trained from collocated observations between ATMS-NPP and CloudSat cloud profiling radar (CPR) snowfall product. Both brightness temperature (TB) variables and global forecast system (GFS) output variables are evaluated for snowfall detection in this algorithm. Results show that combining TB variables and GFS variables provide the optimal snowfall detection performance. The Heidke skill score (HSS) values are about 0.56 over all three surface types, and the probability of detection (POD) values are 0.76, 0.70, and 0.72 over ocean, sea ice, and coast, respectively. The importance of the GFS variables differs greatly among these three surface types. The detection algorithm primarily depends on TB variables over ocean and HSS only increased by 0.05 by adding GFS variables. In contrast, GFS variables are critically important to snowfall detection over sea ice and coastal regions. Without GFS variables, the HSS values over both sea ice and coastal regions decrease sharply from about 0.56 to about 0.40. Over ocean, we also developed a regional snowfall detection model in each 10° grid box, which greatly outperform the global detection model over certain regions (e.g., sea of Okhotsk and Labrador Sea). Case studies and validation against NOAA-20 observations showed that the snowfall detection algorithm performs well, which will benefit coastal communities by providing information on snowstorms offshore before they transition to land.

Index Terms—Microwave radiometry, satellite applications, snow.

I. INTRODUCTION

SNOWFALL accounts for a large fraction of precipitation occurrence in the middle and high latitudes [1]–[6]. Satellite observations provide the only means to measure snowfall on the global scale, especially over ocean where traditional instruments (e.g., ground radar and gauge) are almost nonexistent.

The CloudSat cloud profiling radar (CPR) with a minimum detection reflectivity at ∼-30 dBZ has long been used for snowfall research [1], [2], [7]–[11]. Liu produced an observation-based global snowfall map from one year CPR observations [1], which showed that over the Southern Ocean heavy snowfall events most frequently occur in the latitudinal band centered around 60°S, while in the Northern Hemisphere, heavy snowfall events over ocean often occur over several specific regions (e.g., Sea of Okhotsk, Labrador Sea, and the Ocean East of Greenland, and North Europe and Arctic Ocean). Snowfall morphology analyses revealed that shallow snowfall events with cloud top less than 4 km occur predominantly over ocean [12]. Previous studies demonstrated that snowfall derived from CPR observations agree well with that from ground radar [7], [9], [13], [14], and reanalysis datasets [15], [16].

The dual frequency radar (DPR) onboard the global precipitation measurement (GPM) core observatory satellite has also been used to investigate the snowfall characteristics. Adhikari *et al.* [5] investigated the snowfall features using three years of GPM DPR observations. They noticed obvious differences between snowfall in the Northern Hemisphere and Southern Hemisphere (e.g., stronger diurnal and seasonal variation over Northern Hemisphere), and between snowfall over land and ocean (e.g., more intense snowfall over land). Comparison studies between GPM DPR and CloudSat CPR revealed that DPR misses 90% of snowfall events relative to CPR [2], [17] due to its much larger minimum detection reflectivity at ∼12 dBZ [18], compared with that from CPR of −30 dBZ.

Many previous studies also demonstrated the capability of passive microwave radiometers for snowfall detection, including Special Sensor Microwave/Imager (SSM/I) and SSM/Temperature 2 (SSM/T2) [19], Advanced Microwave Sounding Unit-B (AMSU-B) [20]–[22], Special Sensor Microwave Imager/Sounder (SSMIS) [23], [24], GPM Microwave Imager (GMI) [6], [24]–[28], Microwave Humidity Sounder (MHS) [22], [29], advanced technology microwave sounder (ATMS) [30]–[32]. These previous studies pointed out that the high frequency channels (≥85 GHz) are indispensable for snowfall detection, which has also been confirmed by theoretical studies [33]–[36]. You *et al.* [37] showed that snowfall probability of detection (POD) decreases sharply from 0.77 to 0.35 without the high frequency channels.

Compared with spaceborne radars, there are several challenges with using passive microwave radiometers for snowfall detection, including the highly variable surface emissivity over

snow covered land regions and sea ice [22], [38], [39], super-cooled cloud liquid water causing brightness temperature (TB) to increase and obscuring the TB depression signature from ice scattering [29], [40]–[42], and the indirect relationship between surface snowfall rate and the hydrometeors in the air [43]. However, there are more than 10 passive microwave radiometers currently operational and suitable for snowfall studies [44], [45], while GPM DPR is the only operational spaceborne radar capable of detecting heavy snowfall events. More importantly, passive microwave radiometers provide much wider spatial coverage (e.g., ∼245 km from DPR vs. ∼2500 km from ATMS). The availability of these radiometers along with their wider spatial coverage are critical to generate the 3-hourly and finer scale global precipitation dataset [44], [46], [47].

Parameters from reanalysis datasets and/or numerical model outputs have also been used to further improve the snowfall detection performance. For example, You *et al.* showed that vertical velocity and relative humidity in lower troposphere can increase snowfall POD by about 10% over the contiguous United States (CONUS) [23]. An overland snowfall detection algorithm from Kongoli *et al.* [48] used surface relative humidity and 2-m air temperature to filter out unlikely snowfall pixels from ATMS in the dry and warm scenarios. They further improved this overland snowfall detection algorithm by including more ancillary variables from NOAA's GFS model (e.g., cloud thickness, cloud top and base heights, cloud top and base temperatures, relative humidity, and vertical velocity at different levels) [32]. They concluded that the optimal snowfall detection performance is obtained when combining the information from ancillary GFS variables and satellite TB observations.

ATMS is a key instrument in the joint polar satellite system (JPSS, the latest generation of NOAA's polar-orbiting environmental satellite program), which was first launched onboard the NPP satellite in 2011, followed by N20 (JPSS-1) in 2017. ATMS is expected to be onboard JPSS-2 in 2022, JPSS-3 in 2026, and JPSS-4 in 2032 [49]. Meng *et al.* [31] developed a snowfall retrieval algorithm for passive microwave radiometers, which provides the operational snowfall products over land for ATMS. The objective of this study is to develop a snowfall detection algorithm over ocean, sea ice, and coast for ATMS onboard both Suomi-NPP (NPP) and NOAA-20 (N20) satellites. This study is an extension of the current NOAA's operational snowfall products over land [31]. Currently, the logistic regression method is used for snowfall detection over land [31], [32], which has also been adopted for the snowfall detection over ocean, sea ice, and coast. Key innovations include that 1) this study uses the CloudSat snowfall estimates as the "reference (truth)"; and 2) we quantify the snowfall detection skills from both ATMS TB observations and GFS ancillary variables, and explain where and why both variables are necessary for optimal snowfall detection performance.

II. DATASETS

A. ATMS Brightness Temperature From NPP and N20

ATMS scans cross-track $\pm 52.8°$ relative to nadir at ∼824-km altitude with 22 channels and 96 field-of-view (FOV) samples from each scan line. This study selected 11 channels

TABLE I
SELECTED 11 CHANNELS AND THEIR RESOLUTIONS AT NADIR FOR SNOWFALL DETECTION ALGORITHM DEVELOPMENT FROM THE ATMS

Frequency (GHz)	Abbreviation	Resolution (km)
23.8 (QV)	24	75
31.4 (QV)	31	75
52.8 (QH)	53	32
53.596±0.115 (QH)	54	32
88.2 (QV)	88	32
165.5(QH)	166	16
183.31±1 (QH)	183±1	16
183.31±1.8 (QH)	183±2	16
183.31±3 (QH)	183±3	16
183.31±4.5 (QH)	183±5	16
183.31±7 (QH)	183±7	16

The QV and QH stand for quasi-vertical and quasi-horizontal polarizations, respectively.

that are related to precipitation process for snowfall algorithm development. They are 23.8 (QV), 31.4 (QV), 52.8 (QH), 53.596 ± 0.115 (QH), 88.2 (QV), 165.5 (QH), 183.31 ± 1 (QH), 183.31 ± 1.8 (QH), 183.31 ± 3 (QH), 183.31 ± 4.5 (QH) and 183.31 ± 7 (QH) GHz (QV=quasi-vertical and QH=quasi-horizontal polarizations). Hereafter, these channels are referred to as V24, V31, …, and H183.3 ± 7 for convenience. The horizontal resolution at nadir is about 75 km for 24 and 31 GHz, 32 km for channels at ∼50 and 88 GHz, and 16 km for 166 and 183 GHz channels. This information is summarized in Table I.

As a cross-track scanning sensor, the footprint size increases from the center of the scan line to the edge. For example, the FOV size at nadir at H166 GHz is about 16 km, while it is 68×30 km at the edge of the swath. We stratify these pixels into three categories (center, middle, and edge) to match with CloudSat snowfall product (more details in the Section III).

This study uses the TB observations from January 2012 (three months after the NPP launch) to July 2019 (end date of the CPR snowfall product) from NPP, and January 2018 (two months after the N20 launch) to July 2019 from N20, respectively. Due to the limited matchup samples between N20 and CloudSat, we trained the snowfall detection algorithm using matchups between NPP and CloudSat, while applying the detection algorithm to both NPP and N20. The matchup samples between N20 and CloudSat are used as an independent dataset to validate the snowfall detection algorithm's performance. From now on, we use ATMS to represent either ATMS-NPP, or ATMS-N20, or both sensors, depending on the context.

B. CloudSat Snowfall Data

CloudSat CPR is a nadir-looking radar with a spatial resolution of 1.4×1.8 km and vertical resolution of 500 m [50]. It is arguably the most reliable snowfall measurement instrument on the global scale [10]. This study uses the latest version (V05) CPR snowfall product as the "reference (truth)" from January 2012 (three months after the launch of the NPP satellite) to July 2019 (end date of the CPR snowfall product). Specifically, we obtained three variables from 2C-SNOW-PROFILE product, including surface snowfall rate ($snowfall\_rate\_sfc$), snowfall rate profile ($snowfall\_rate$), and snow water content profile

(*snow_water_content*). Only the data of good quality, as indicated by the "data quality" variable in 2C-SNOW-PROFILE product being 0, are retained.

C. GFS and Other Ancillary Variables

As previous studies demonstrated, the environmental parameters from numerical weather prediction model outputs (e.g., relative humidity) contain valuable snowfall detection information [23], [32]. In addition to the ATMS TB observations, this study assesses 115 parameters from GFS for possible snowfall detection improvements. The selected variables are listed in Table I. The spatial and temporal resolutions for GFS analysis variables are 0.5° and 6-hourly (00, 06, 12, and 18 UTC), respectively. To increase the temporal resolution, we also use the forecast fields at 03, 09, 15, 21 UTC. That is, the temporal resolution becomes 3-hourly when combining the analysis and forecast fields.

We also use the precipitation rate data from the multiradar multisensor (MRMS) system in two case studies, which is at 1-km and 2-min spatial and temporal resolutions, respectively [51]. It is worth mentioning that MRMS data are only available over the CONUS and near coastal regions. A radar quality index (RQI) is also developed to represent the MRMS precipitation data quality [52]. It is shown later that the RQI decreases dramatically away from land areas.

The sea ice coverage information is obtained from the 4-km daily global multisensor automated snow/ice cover map [53]. The surface type (i.e., land, ocean, and coast) definition is based on the 1-km land elevation data [54] by considering each ATMS pixel's ellipse boundary on the earth surface (more details in following collocation scheme section).

III. METHODOLOGY

A. Collocation Scheme

As mentioned previously, there are three spatial resolutions for the selected 11 ATMS channels. We take the resolution at 166 GHz (16 km at nadir) as the nominal resolution. The lower resolution TB at other channels (i.e., from 24 to 88 GHz) remains unchanged. To consider the varying foot print size from central to the edge scan line, we stratify the 96 FOV footprints in each scan line into three categories, including central from scan position 20–77, middle from scan position 10–19 and 78–87, and edge from scan position 1–9 and 88–96.

For each ATMS pixel, we first check whether there are CPR pixels within 15 min time difference with the ATMS pixel. If there are CPR pixels close in time (i.e, <15 min) with a ATMS pixel, we average all CPR pixels within an area with radius being 9, 12, and 18 km for central, middle, and edge categories, respectively. The 9, 12, and 18 km are roughly the effective ATMS radius dividing the CPR pixel resolution (e.g., 16/1.8≈9) in each group. It is worth mentioning that we choose theses threshold values (i.e., 9 km, 12 km, 18 km, and 15-min) to balance the matchup accuracy and the matchup sample size. To attach GFS variables to each collocated ATMS-CPR pixel, we first find the closest GFS grid for each ATMS-CPR pixel, then linearly interpolate each variable in the temporal dimension. It is worth mentioning that the temporal and spatial resolutions are 3-h and 0.5° for GFS variables.

First, ocean and coast pixels are separated based on the ocean percentage in each ATMS pixel; and then the sea ice pixels are further identified from the ocean category. Specifically, within each ATMS ellipse boundary, we compute the percentage of the ocean from the 1 km land elevation data, where the land region has an elevation value greater than 0, while a negative value is assigned to the oceanic surface. A surface type of a pixel is determined as ocean when at least 80% of the ellipse is covered by ocean. The surface type of a pixel is labeled as coast if the percentage of ocean in the ellipse is less than 80%, but greater than 20%. For each ocean ATMS pixel, it is further classified as over sea ice (ocean) if half of the pixel area is covered by sea ice (ocean) based on the 4-km daily snow/ice cover data.

B. Logistic Regression

To determine the snowfall status of each pixel, we use the logistic regression model, which has been used over land for snowfall detection in the NOAA's operational ATMS retrieval algorithm [31], [48]. This study combines information from TB channels and GFS variables for optimal snowfall detection performance over ocean, sea ice, and coast. Two training databases (i.e., snow vs. no-snow pixels) are required with each of them containing multivariables x (e.g., relative humidity, total precipitable water, and H183 ± 7). According to [55], snowfall probability p can be computed with the following equation:

$$ln\left(\frac{p}{1-p}\right) = b_0 + b_1 x_1 + \cdots + b_k x_k \tag{1}$$

where p stands for snowfall probability. x_i represents the ith selected variable ($i = 1, \ldots, k$) and k is the total number of variables. In the final selected model, this number (k) is 13, 17, and 18 over ocean, sea ice, and coast, respectively. We provide a case study in the Section IV to further illustrate how we use logistic regression for snowfall detection.

C. Evaluation Metrics

To assess the snowfall detection performance, four numbers in a 2 × 2 contingency table (hit, miss, false alarm, and correct negative) are computed [55]. A hit is defined as both CPR and the ATMS detection algorithm detecting snowfall. A false alarm is when the ATMS algorithm detects snowfall, while CPR does not, while a miss is when the CPR detects snowfall but the ATMS detection algorithm does not. A correct negative is when both CPR and the ATMS detection algorithm detect no snowfall. These four numbers are referred to as hit number 1), false alarm number 2), miss number 3), and correct negative number 4). This study computes the accuracy metrics derived from these four numbers, including POD, false alarm ratio (FAR), and HSS.
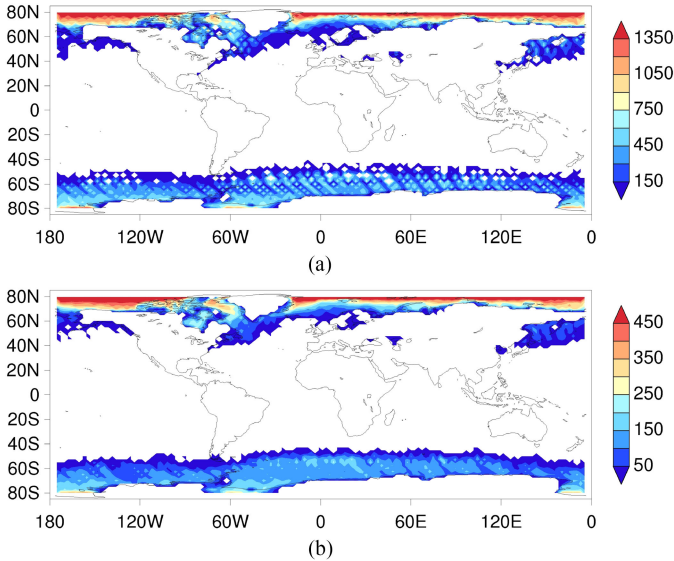
Fig. 1. (a) Geospatial distribution of the collocated ATMS-NPP and CPR samples from 2012 to 2019 in each 2.5° grid box over ocean, sea ice, and coast. (b) Same as (a) except for ATMS-N20 from 2017 to 2019.
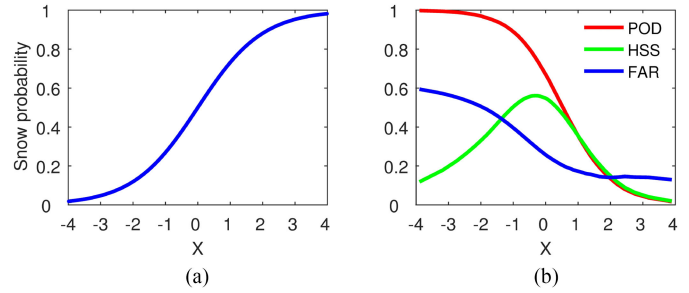

Fig. 2. (a) Snowfall probability derived from the logistic regression over ocean, corresponding to different predictor values (i.e., $x = b_0 + b_1 x_1 + \cdots + b_k x_k$) in the x-axis. (b) Detection metrics, including POD, FAR, and HSS over ocean, corresponding to different predictor values in the x-axis.

For ATMS-N20, the sample sizes are 148 501, 253 534, 20 547, over ocean, sea ice, and coast, respectively.

B. Logistic Regression Demonstration Over Ocean

Fig. 2 provides a demonstration of the logistic regression snowfall detection approach by showing the snowfall probability [see Fig. 2(a)] and the evaluation metrics [Fig. 2(b)], deriving from matchup samples between ATMS-NPP and CloudSat CPR over ocean. Predictor variables include V24, V31, H53, H54, all high frequency channels (V88, H166, and five H183 channels), relative humidity at 900 hPa, and cloud liquid water (CWAT). We explain in the next section how and why these variables are selected. Apparently, choosing different threshold values of x [right side of (1), shown as x-axis values on Fig. 2(a) and (b)], the snowfall probability and the evaluation metrics vary accordingly. In particular, the large POD value is almost always associated with a large FAR value, except when both values are less than ∼0.2 [see Fig. 2(b)]. For this reason, we select HSS as an overall performance metrics. The threshold value for x is selected when HSS peaks. For this case, the HSS value peaks at 0.56 [green curve in Fig. 2(b)], corresponding to the threshold value of x being −0.32 on the x-axis in Fig. 2(b). Based on the (1), the corresponding snowfall probability value is 0.42 with x being −0.32.

These metrics are calculated as follows:

$$\text{POD} = \frac{a}{a+c}$$

$$\text{FAR} = \frac{b}{a+b}$$

$$\text{HSS} = \frac{2(ad-bc)}{(a+c)(c+d)+(a+b)(b+d)}. \tag{2}$$

The POD (FAR) values vary from 0 to 1 with a larger POD (smaller FAR) indicating better detection performance. A large POD value is often associated with a large FAR value, which makes it difficult to directly compare detection performance using POD or FAR. For this reason, this study uses the Heidke skill score (HSS) value (varying from −∞ to 1) to evaluate the overall detection performance with a larger HSS value indicating a better overall performance. An HSS value greater than zero indicates a performance better than random chance.

IV. RESULTS

A. Geospatial Distribution of Collocated CPR and ATMS

Fig. 1 shows the geospatial distribution of matchups between CPR and ATMS-NPP [see Fig. 1(a)], and between CPR and ATMS-N20 [see Fig. 1(b)] over ocean, sea ice, and coast in each 2.5° grid box. It is worth mentioning that these are matchup samples filtered using the precipitation phase determination approach [56]. Specifically, the wet-bulb temperature scheme is used for this screening. In other words, we first discard ATMS pixels under warm temperature scenarios unlikely associated with snowfall. This explains why few matchup samples show up in the 40°S to 40°N latitudinal band.

Overall, there are 424 921, 788 100, 60 322 matchups between CPR and ATMS-NPP over ocean, sea ice, and coast, respectively.

C. Variable Selection

First, all 11 TB channels are used for physical reasons over all three surface types (ocean, sea ice, and coast), which are V24, V31, H53, H54, V88, H166, and five H183.3 GHz channels. Previous studies showed that the high frequency channels are indispensable for snowfall detectio, since they are able to capture the ice scattering signature [33]–[37]. The low frequency channels at 24 and 31 GHz are chosen since they provide the surface emission background, which is subject to large variabilities, especially over sea ice and coastal regions [39]. The channel around 50 GHz is temperature sounding channels in troposphere, providing temperature information close to the surface. It is worth mentioning that the temperature sounding channel at 53 GHz is currently used in the NOAA's operational snowfall detection product over land [31].

TABLE II
THESE ARE GFS VARIABLES TESTED FOR POSSIBLE SNOWFALL DETECTION
IMPROVEMENTS, COMBINING WITH THE ATMS BRIGHTNESS TEMPERATURE
(TB) OBSERVATIONS

Variable Name	Symbol in GFS	Levels
Relative humidty	RH	19
Cloud mixing ratio	CLWMR	19
Vertical velocity	VVEL	19
Geopotential height	HGT	19
Temperature	TMP	19
Mean Sea Level Pressure	MSLET	1
Surface Geopotential height	HGT surface	1
Surface temperature	TMP surface	1
2-meter air temperature	TMP 2 m above ground	1
Relative humidity at 2-meter	RH 2 m above ground	1
Entire relative humidity	RH entire atmosphere	1
U-component wind at 10-meter	UGRD 10 m above ground	1
V-component wind at 10-meter	VGRD 10 m above ground	1
Specific humidty at 2 meter	SPFH 2 m above ground	1
Lifted index	LFTX	1
CAPE surface	CAPE surface	1
CAPE 180 hPa above ground	CAPE 180 hPa above ground	1
CAPE 250 hPa above ground	CAPE 250 hPa above ground	1
CIN surface	CIN surface	1
CIN 180 hPa above ground	CIN 180 hPa above ground	1
CIN 250 hPa above ground	CIN 250 hPa above ground	1
U-component of storm motion	USTM	1
V-component of storm motion	VSTM	1
Precipitable water	PWAT	1
Cloud water	CWAT	1
Total variable count		115

Among these variables, there are five profiles at 19 pressure levels (From 200 to 900 Hpa with a 50 Hpa increment, 925 Hpa, 950 Hpa, and 1000 Hpa,), including relative humidity, cloud mixing ratio, geopotential height, temperature. All other variables are one dimensional.
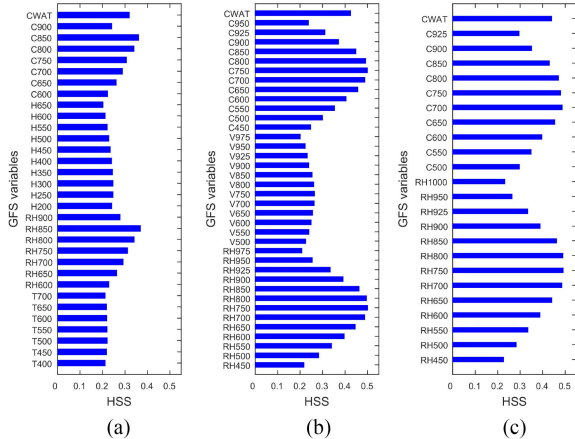

Fig. 3. (a) GFS variables with a HSS value at least 0.2 over ocean. (b) Same as (a) except over sea ice. (c) Same as (a) except over coast. (T=Temperature, RH=relative humidity, H=Geopotential height, C=Cloud mixing ratio, V=Vertical velocity, and CWAT=total cloud water. The numbers stand for the pressure level in the unit of hPa). The total GFS variable number with a HSS value at least 0.2 is 32, 38, and 24, over ocean, sea ice, and coast, respectively.

Second, all GFS variables listed in Table II are tested individually using the method shown in Fig. 2. We only select the GFS variables with a HSS value of 0.2 or larger. The selected GFS variables over three surface types are shown in Fig. 3. It is found that the selected GFS variables are closely related to the precipitation process, including relative humidity, temperature, geopotential height, vertical velocity, and cloud mixing ratio

TABLE III
FINAL RESULTS OF VARIABLE SELECTION OVER OCEAN, SEA ICE, AND COAST

	GFS variables
ocean	RH900, CWAT
Sea ice	RH850, RH900, RH925, RH950, RH975 , CWAT
Coast	RH750, RH850, RH900, RH925, RH950, RH1000, CWAT

We use 11 TB variables over all three surface types, including V24, V31, H53, H54, H88, H166, and 183.3 ± 7, 5, 3, 2,1. Only the selected GFS variables are listed in the Table. RH represents relative humidty. CWAT is total cloud water
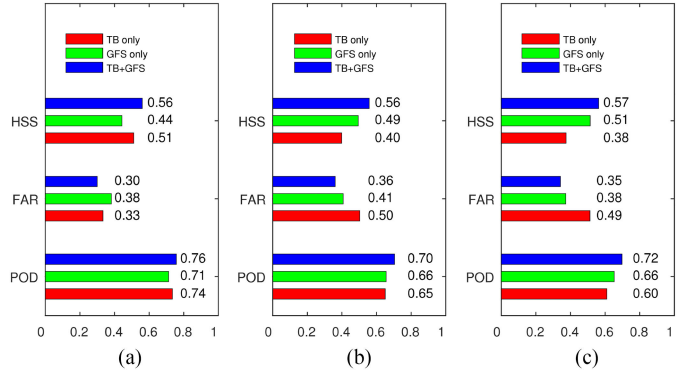

Fig. 4. (a) The snowfall detection metrics, including POD, FAR, and HSS over ocean by using TB variables, GFS variables, and both TB and GFS variables. (b) Same as (a) except over sea ice. (c) Same as (a) except over coast.

at different pressure levels, and CWAT (total cloud water). In addition, it is shown that relative humidity and cloud mixing ratio in the lower troposphere (e.g., 850 hPa) has very strong snowfall detection capability over sea ice and coast, indicated by a HSS value of ∼0.5 [see Fig. 3(b) and (c)].

Third, the selected variables with HSS at least being 0.2 are added to the 11 TB variables in a stepwise manner. Specifically, we first compute the HSS value using the 11 TB variables. Then, we recompute the HSS value by adding the selected GFS variables one by one. If the HSS value increases by at least 0.02 when adding a certain variable, it is retained. Otherwise, that variable is discarded. The final results are listed in Table III. Clearly, over both sea ice and coast surface, more GFS variables are needed to achieve the optimal snowfall detection performance. In addition, it is noted that the selected variables are correlated to each other (e.g., the high frequency TB channels, and the relative humidity at different pressure levels). We also use the principal component analysis (PCA) approach to address the multicollinearity issue among the selected variables. Further analyses show that the detection statistics from the PCA approach is worse than our current scheme, especially over coast.

D. Detection Performance From TB and GFS

Fig. 4 shows the detection statistics over ocean, sea ice, and coast. We compute the detection metrics using TB and GFS variables to quantify how much detection information is contained in each variable type (i.e., TB vs. GFS variables, Table II). The detection metrics are also calculated by using both TB and GFS variables shown in Table III. In the calculation process, we randomly divide the data into the training subset (80% of

data) and the validation subset (20% of the data). The following metrics values are computed from the validation subset.

Over ocean, the POD, FAR, and HSS values are 0.74, 0.33, and 0.51 when only using the 11 TB variables [see Fig. 4(a)]. By only using GFS variables (RH at 900 hPa and CWAT in Table III), the detection performance is noticeably worse than that from only using TB variables, indicated by smaller POD and HSS values, and a larger FAR value. Combining TB and GFS variables, the detection statistics slightly improve, compared with those from TB variables only. For example, the HSS vale increase from 0.51 to 0.56 [see Fig. 4(a)] by adding GFS variables.

In contrast, over both sea ice [see Fig. 4(b)] and coast [see Fig. 4(c)], the detection performance is better by only using GFS variables than by only using TB variables. For example, over coast, the HSS value is 0.51 from GFS variables, while it is only 0.38 from TB variables. It basically means that GFS variables alone can provide more detection capability than the TB variables [cf. The red bars and green bars in Fig. 4(b) and 4(c)]. More importantly, by combining the TB and GFS variables, we can obtain the optimal snowfall detection performance, indicated by better detection statistics. The reason why GFS variables add more detection information over sea ice and coast is likely because the complex surface background (e.g., large surface emissivity variation over sea ice and mixed land-ocean pixels over coast) can obscure the hydrometeors signature in the TB observations. In contrast, the surface emissivity over ocean is much more homogeneous than over sea ice and coast. The detection result over sea ice and coast highlights the importance of adding the GFS variables when using passive microwave radiometers for snowfall detection over complex surface types.

E. Regional Model Performance

In the previous section, we demonstrated the snowfall detection performance trained with the global dataset. Considering the regional differences in snowfall characteristics, we further trained a logistic regression model in each $10°$ grid box over ocean using the GFS variables shown in Table III and 11 TB variables. To ensure the stability of the logistic regression model, it is required that at least 2500 collocated ATMS and CPR pixels with snowfall rate greater than 0 are in each $10°$ grid box. If not, we expand the grid box by $5°$ at a time until this sample size requirement is met.

Fig. 5 shows the geospatial distribution of the three evaluation metrics (POD, FAR, and HSS) in each $10°$ grid box over ocean. It is immediately clear that the detection performance is better over several regions in the Northern hemisphere, indicated by larger POD and HSS values, and small FAR values. These regions include Labrador Sea, ocean surface west of Greenland, and sea of Okhotsk. The histogram plots (see Fig. 6) further corroborate that the certain regions have better detection statistics than using the global model. For example, about half of the grid boxes have a HSS value greater than 0.56 [vertical dash line in Fig. 6(c), the value from the global model].

To understand why these regions have a better snowfall detection performance, we select two regions [green boxes shown in Fig. 5(a): Area 1 (40°–82°N, 20°–70°W], where snowfall
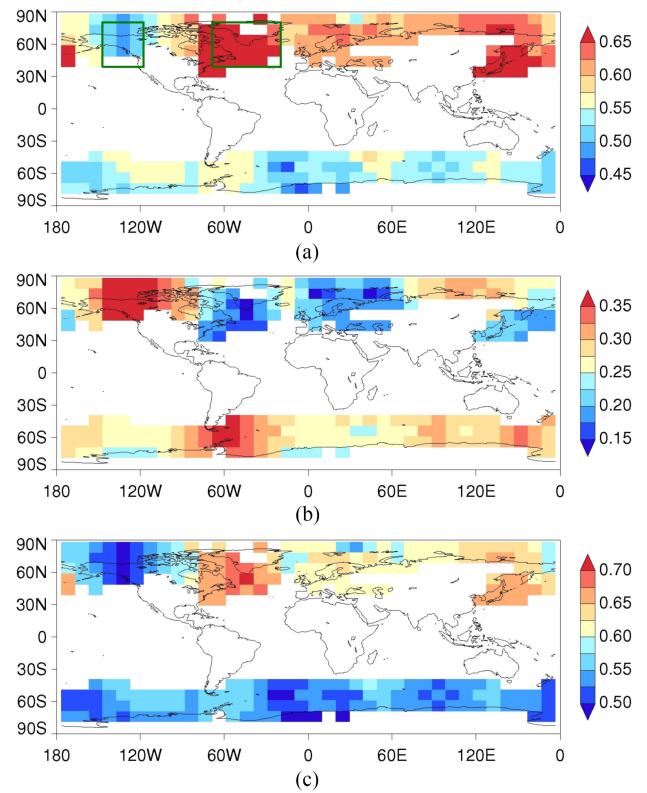

Fig. 5. (a) Geospatial distribution of the POD in each $10°$ grid box. (b) Same as (a) except for FAR. (c) Same as (a) except for HSS. Further analyses are performed in the two green boxes in Fig. 5(a) to explain why there exists regional snowfall detection performance differences, which is shown in Fig. 7.
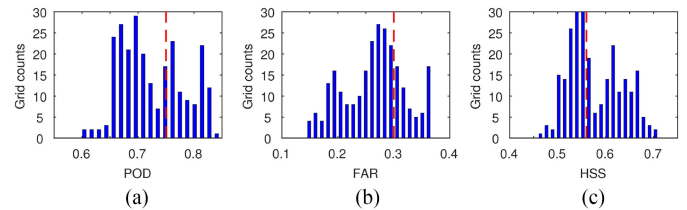

Fig. 6. (a) Histograms of POD in each $10°$ grid box. (b) Same as (a) except for FAR. (c) Same as (a) except for HSS. The dashed vertical line in each subplot corresponds to the value from the global model.

detection performance from $10°$ regional model is much better than that from the global model, and Area 2 (40°–82°N,120°–150°W), where snowfall detection performance from the $10°$ regional model is noticeably worse than that from global model. Fig. 7 shows the average snowfall and ice water content profiles, and the histograms from H166 in these two regions, corresponding to all snowfall rate greater than 0. Obviously, the average snowfall rate and water content profiles are consistently larger in Area 1 than in Area 2. In other words, snowfall rates over Area 1 tend to be heavier than that in Area 2. In fact, the ice water path [integrating the ice water content profile in Fig. 7(b)] in Area 1 is 268 g/m^2, while it is only 146 g/m^2 in Area 2. The much larger ice water path in Area 1 results in a colder brightness temperature, as clearly demonstrated in Fig. 7(c) of the H166
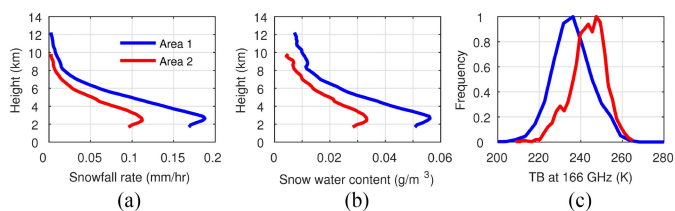
Fig. 7. (a) Mean snowfall profile in the two selected areas (Area 1: (40°–82°N, 20°–70°W); Area 2: (40°–82°N, 120°–150°W), indicated by the two green boxes in Fig. 5. (b) Mean water content profiles in the two selected areas. (c) Histograms of H166 under snowfall scenarios in the two selected areas.

histogram. Specifically, the average H166 with snowfall rate greater than 0 is 235 K in Area 1, while Area 2 has a much warmer average H166 at 248 K. The colder TB due to the heavier snowfall rate in Area 1 makes it relatively easier to detect. To consider the regional difference, we choose to use a regional logistic regression model for a given 10° grid box when the HSS value in that grid box is at least 0.05 larger than the HSS value from the global model (i.e., 0.56).

Over sea ice, similar analyses are performed with no superior performance of using a regional model being noticed. Further analyses show that the large emissivity variations over different ages of sea ice may explain why the regional models over sea ice do not outperform the global model. This is a topic for future study. We do not train any regional model over coast due to the limited sample size.

F. Snowfall Detection Algorithm Validation

To validate our snowfall detection algorithm's performance, this section first demonstrates two case studies from ATMS-N20 and ATMS-NPP over the northeast coast of United States on January 31 2021. Additionally, we also show the overall detection metrics derived from the collocated N20-CloudSat data set. It is worth mentioning that our detection algorithm is trained on the NPP-CloudSat dataset. Therefore, N20-CloudSat collocated samples can be considered as an independent validation dataset.

Fig. 8(a) shows two high snowfall probability regions (over the New Jersey coast and the ocean east of the Massachusetts) derived from ATMS-N20 on January 31 2021 at 17:36 UTC. These two snowfall regions are clearly identified after filtering the no-snow pixels [see Fig. 8(b)]. Part of the snowfall event over the New Jersey coast has also been observed by the MRMS, shown in Fig. 8(c). However, the quality of the MRMS precipitation rate decreases dramatically further away from the radar site, indicating by the RQI quickly decreasing to 0 over ocean [see Fig. 8(d)]. Evidently, the snowfall pixels over the ocean east of the Massachusetts is well beyond the MRMS's coverage, which highlights the valuable information provided by the ATMS observation.

This snowfall system was also observed by the ATMS-NPP on January 31 2021 at 18:26 UTC. Similarly, ATMS-NPP clearly captured the two high snowfall probability regions over the New Jersey coast and over the ocean east of the Massachusetts [see Fig. 9(a) and (b)]. MRMS only detected part of the snowfall event over the New Jersey coast [see Fig. 9(c)]. More importantly, the
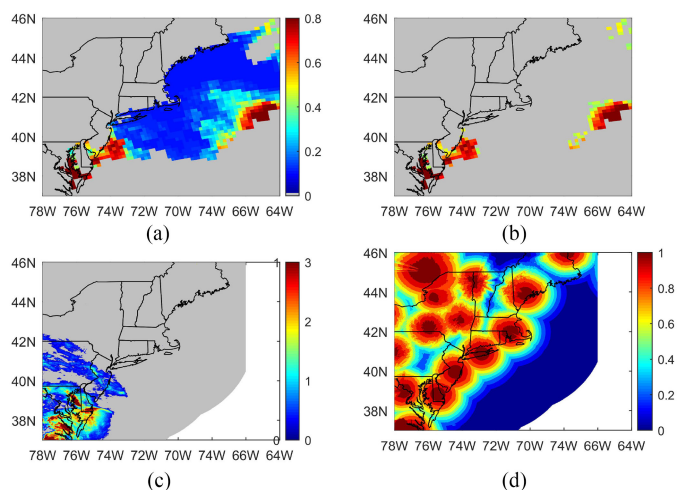

Fig. 8. (a) Snowfall probability derived from ATMS-N20 on January 31, 2021 at 17:36 UTC over the northeast coast of United States. (b) Snow pixels after using the threshold values (i.e., filtering out no-snow pixels). (c) Precipitation rates estimated from MRMS on January 31 2021 at 17:36 UTC. (d) The RQI for the MRMS estimated precipitation rates on January 31 2021 at 17:36 UTC.
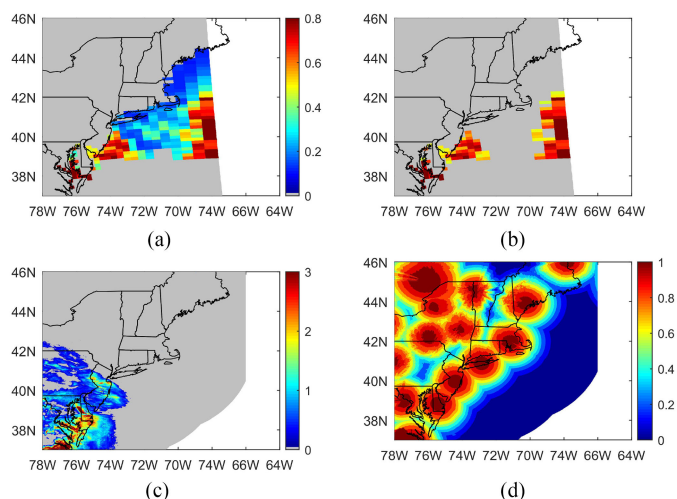

Fig. 9. (a) Snowfall probability derived from ATMS-NPP on January 31 2021 at 18:26 UTC over the northeast coast of United States. (b) Snow pixels after using the threshold values (i.e., filtering out no-snow pixels). (c) Precipitation rates estimated from MRMS on January 31 2021 at 18:26 UTC. (d) The RQI for the MRMS estimated precipitation rates on January 31 2021 at 18:26 UTC.

snowfall pixels over the ocean east of the Massachusetts are completely beyond the MRMS's coverage [see Fig. 9(d)].

Comparing these two cases from ATMS-N20 [see Fig. 8] and ATMS-NPP [see Fig. 9], it is evident that the snowfall event over the ocean east of the Massachusetts was approaching the densely populated metropolitan areas (e.g., Boston and New York). This information is critically important for the coastal communities since satellite detected snowstorms offshore before they transition to land. In particular, satellite observations can provide situational awareness to forecasters in their support of such activities like US Coast Guard search and rescue and other aviation activities.

TABLE IV
DETECTION METRICS BY APPLYING THE SNOWFALL DETECTION ALGORITHM
DEVELOPED FOR ATMS-NPP TO THE MATCHUPS BETWEEN ATMS-N20 AND
CPR FROM 2017 TO 2019

	POD	FAR	HSS
ocean	0.79	0.35	0.56
Sea ice	0.72	0.38	0.54
Coast	0.72	0.37	0.55

Next, we apply the snowfall detection algorithms over these three surface types to the independent ATMS-N20 matchup dataset with CPR from 2017 to 2019. The detection performance over these three surface types is very similar to those from ATMS-NPP matchup dataset. Specifically, the HSS values are about 0.56 and the POD values are greater than 0.70 over all three surface types (see Table IV).

V. CONCLUSION

A set of snowfall detection algorithms are developed in this study for over ocean, sea ice, and coast for ATMS onboard NPP and N20, using the CloudSat CPR estimated snowfall product as the "reference (truth)." Both TB variables and ancillary variables from GFS numerical weather prediction model analysis and forecast are tested for their snowfall detection capability. It is found that both TB and GFS variables are necessary to achieve the optimal snowfall detection performance over all three surface types.

However, the importance of the GFS variables differs greatly among these three surface types. Over ocean, TB variables provide the vast majority of the snowfall detection information with a HSS value of 0.51. Adding the GFS variables only increases the HSS value from 0.51 to 0.56. In contrast, GFS variables possess better snowfall detection capability than that of TB variables, indicated by larger HSS values. For example, over coastal region, the HSS value from TB variables is 0.38, while it is 0.51 from GFS variables.

To account for the regional snowfall characteristics, we also develop a regional model in each 10° box over ocean. It is found that over several regions in the Norther Hemisphere (e.g., Labrador sea and sea of Okhotsk), the regional models clearly outperform the global model. The final selected model over ocean is a mixture of the global and regional models. Specifically, we use the regional models over a given 10° grid box if the HSS value in that grid is at least 0.05 greater than that from the global model. No clear advantage of the regional models is noticed over sea ice most likely due to the highly variable surface emissivity over sea ice. Therefore, the global model is used over sea ice. The global model is also applied over coast due to the insufficient amount of data for model training.

Case studies and validation against ATMS-N20 observations showed that the snowfall detection algorithm performs well, which will benefit coastal communities by providing information on snowstorms offshore before they transition to land. Future work includes the development of snowfall rate algorithms for ATMS over the three surface types.

REFERENCES

[1] G. Liu, "Deriving snow cloud characteristics from cloudsat observations," *J. Geophys. Res., Atmos.*, vol. 113, no. D8, 2008.

[2] M. S. Kulie and R. Bennartz, "Utilizing spaceborne radars to retrieve dry snowfall," *J. Appl. Meteorol. Climatol.*, vol. 48, no. 12, pp. 2564–2580, 2009.

[3] A. Behrangi, Y. Tian, B. H. Lambrigtsen, and G. L. Stephens, "What does cloudsat reveal about global land precipitation detection by other spaceborne sensors," *Water Resour. Res.*, vol. 50, no. 6, pp. 4893–4905, 2014.

[4] G. Skofronick-Jackson *et al.*, "Global precipitation measurement cold season precipitation experiment (GCPEX): For measurement's sake, let it snow," *Bull. Amer. Meteorol. Soc.*, vol. 96, no. 10, pp. 1719–1741, 2015.

[5] A. Adhikari, C. Liu, and M. S. Kulie, "Global distribution of snow precipitation features and their properties from 3 years of GPM observations," *J. Climate*, vol. 31, no. 10, pp. 3731–3754, 2018.

[6] L. Milani *et al.*, "Extreme lake-effect snow from a GPM microwave imager perspective: Observational analysis and precipitation retrieval evaluation," *J. Atmos. Ocean. Technol.*, vol. 38, no. 2, pp. 293–311, 2021.

[7] S. Y. Matrosov, M. D. Shupe, and I. V. Djalalova, "Snowfall retrievals using millimeter-wavelength cloud radars," *J. Appl. Meteorol. Climatol.*, vol. 47, no. 3, pp. 769–777, 2008.

[8] N. B. Wood, T. S. L'Ecuyer, A. J. Heymsfield, G. L. Stephens, D. R. Hudak, and P. Rodriguez, "Estimating snow microphysical properties using collocated multisensor observations," *J. Geophys. Res., Atmos.*, vol. 119, no. 14, pp. 8941–8961, 2014.

[9] L. Norin, A. Devasthale, T. L'Ecuyer, N. Wood, and M. Smalley, "Inter-comparison of snowfall estimates derived from the cloudsat cloud profiling radar and the ground-based weather radar network over Sweden," *Atmos. Meas. Techn.*, vol. 8, no. 12, pp. 5009–5021, 2015.

[10] M. S. Kulie, L. Milani, N. B. Wood, and T. S. L'Ecuyer, "Global snowfall detection and measurement," in *Proc. Satell. Precipitation Meas.*, 2020, pp. 699–716.

[11] L. Milani and N. B. Wood, "Biases in cloudsat falling snow estimates resulting from daylight-only operations," *Remote Sens.*, vol. 13, no. 11, 2021, Art. no. 2041.

[12] M. S. Kulie, L. Milani, N. B. Wood, S. A. Tushaus, R. Bennartz, and T. S. L'Ecuyer, "A shallow cumuliform snowfall census using spaceborne radar," *J. Hydrometeorol.*, vol. 17, no. 4, pp. 1261–1279, 2016.

[13] Q. Cao, Y. Hong, S. Chen, J. J. Gourley, J. Zhang, and P. E. Kirstetter, "Snowfall detectability of NASA's CloudSat: The first cross-investigation of its 2C-snow-profile product and national multi-sensor mosaic QPE (NMQ) snowfall data," *Prog. Electromagn. Res.*, vol. 148, pp. 55–61, 2014.

[14] S. Chen *et al.*, "Comparison of snowfall estimates from the nasa cloudsat cloud profiling radar and NOAA/NSSL multi-radar multi-sensor system," *J. Hydrol.*, vol. 541, pp. 862–872, 2016.

[15] C. Palerme, J. Kay, C. Genthon, T. L'Ecuyer, N. Wood, and C. Claud, "How much snow falls on the antarctic ice sheet," *Cryosphere*, vol. 8, no. 4, pp. 1577–1587, 2014.

[16] L. Milani *et al.*, "Cloudsat snowfall estimates over Antarctica and the Southern Ocean: An assessment of independent retrieval methodologies and multi-year snowfall analysis," *Atmos. Res.*, vol. 213, pp. 121–135, 2018.

[17] D. Casella *et al.*, "Evaluation of the GPM-DPR snowfall detection capability: Comparison with cloudsat-CPR," *Atmos. Res.*, vol. 197, pp. 64–75, 2017.

[18] A. Hamada and Y. N. Takayabu, "Improvements in detection of light precipitation with the global precipitation measurement dual-frequency precipitation radar (GPM DPR)," *J. Atmos. Ocean. Technol.*, vol. 33, no. 4, pp. 653–667, 2016.

[19] G. Liu and J. A. Curry, "Precipitation characteristics in Greenland-Iceland-norwegian seas determined by using satellite microwave data," *J. Geophys. Res., Atmos.*, vol. 102, no. D12, pp. 13987–13997, 1997.

[20] C. Kongoli, P. Pellegrino, R. R. Ferraro, N. C. Grody, and H. Meng, "A new snowfall detection algorithm over land using measurements from the advanced microwave sounding unit (AMSU)," *Geophys. Res. Lett.*, vol. 30, no. 14, 2003.

[21] G. M. Skofronick-Jackson, M.-J. Kim, J. A. Weinman, and D.-E. Chang, "A physical model to determine snowfall over land by microwave radiometry," *IEEE Trans. Geosci. Remote Sens.*, vol. 42, no. 5, pp. 1047–1058, May 2004.

[22] J. L. Foster *et al.*, "Passive microwave remote sensing of the historic February 2010 snowstorms in the middle Atlantic region of the USA," *Hydrol. Processes*, vol. 26, no. 22, pp. 3459–3471, 2012.

[23] Y. You, N.-Y. Wang, and R. Ferraro, "A prototype precipitation retrieval algorithm over land using passive microwave observations stratified by surface condition and precipitation vertical structure," *J. Geophys. Res., Atmos.*, vol. 120, no. 11, pp. 5295–5315, 2015.

[24] C. D. Kummerow *et al.*, "The evolution of the Goddard profiling algorithm to a fully parametric scheme," *J. Atmos. Ocean. Technol.*, vol. 32, no. 12, pp. 2265–2280, 2015.

[25] G. M. Skofronick-Jackson, B. T. Johnson, and S. J. Munchak, "Detection thresholds of falling snow from satellite-borne active and passive sensors," *IEEE Trans. Geosci. Remote Sens.*, vol. 51, no. 7, pp. 4177–4189, Oct. 2013.

[26] J.-F. Rysman *et al.*, "Retrieving surface snowfall with the GPM microwave imager: A new module for the slalom algorithm," *Geophys. Res. Lett.*, vol. 46, no. 22, pp. 13593–13601, 2019.

[27] S. Vahedizade, A. Ebtehaj, Y. You, S. E. Ringerud, and F. J. Turk, "Passive microwave signatures and retrieval of high-latitude snowfall over open oceans and sea ice: Insights from coincidences of GPM and CloudSat satellites," *IEEE Trans. Geosci. Remote Sens.*, vol. 60, pp. 1–13, 2022, doi: 10.1109/TGRS.2021.3071709.

[28] F. J. Turk *et al.*, "Applications of a CloudSat-TRMM and CloudSat-GPM satellite coincidence dataset," *Remote Sens.*, vol. 13, no. 12, 2021, Art. no. 2264.

[29] G. Liu and E.-K. Seo, "Detecting snowfall over land by satellite high-frequency microwave observations: The lack of scattering signature and a statistical approach," *J. Geophys. Res., Atmos.*, vol. 118, no. 3, pp. 1376–1387, 2013.

[30] Y. You, N.-Y. Wang, R. Ferraro, and P. Meyers, "A prototype precipitation retrieval algorithm over land for ATMS," *J. Hydrometeorol.*, vol. 17, no. 5, pp. 1601–1621, 2016.

[31] H. Meng *et al.*, "A 1dvar-based snowfall rate retrieval algorithm for passive microwave radiometers," *J. Geophys. Res., Atmos.*, vol. 122, no. 12, pp. 6520–6540, 2017.

[32] C. Kongoli, H. Meng, J. Dong, and R. Ferraro, "A hybrid snowfall detection method from satellite passive microwave measurements and global forecast weather models," *Quart. J. Roy. Meteorol. Soc.*, vol. 144, pp. 120–132, 2018.

[33] R. Bennartz and P. Bauer, "Sensitivity of microwave radiances at 85-183 GHZ to precipitating ice particles," *Radio Sci.*, vol. 38, no. 4, pp. 40-1–40-8, 2003.

[34] G. M. Skofronick-Jackson *et al.*, "Combined radiometer-radar microphysical profile estimations with emphasis on high-frequency brightness temperature observations," *J. Appl. Meteorol.*, vol. 42, no. 4, pp. 476–487, 2003.

[35] S. D. Michele and P. Bauer, "Passive microwave radiometer channel selection basedoncloudandprecipitation information content," *Quart. J. Roy. Meteorol. Soc.*, vol. 132, no. 617, pp. 1299–1323, 2006.

[36] G. Skofronick-Jackson and B. T. Johnson, "Surface and atmospheric contributions to passive microwave brightness temperatures for falling snow events," *J. Geophys. Res., Atmos.*, vol. 116, no. D2, pp. 729–751, 2011.

[37] Y. You, N.-Y. Wang, R. Ferraro, and S. Rudlosky, "Quantifying the snowfall detection performance of the GPM microwave imager channels over land," *J. Hydrometeorol.*, vol. 18, no. 3, pp. 729–751, 2017.

[38] C. Mätzler, "Passive microwave signatures of landscapes in winter," *Meteorol. Atmospheric Phys.*, vol. 54, no. 1, pp. 241–260, 1994.

[39] S.-M. Lee, B.-J. Sohn, and S.-J. Kim, "Differentiating between first-year and multiyear sea ice in the arctic using microwave-retrieved ice emissivities," *J. Geophys. Res., Atmos.*, vol. 122, no. 10, pp. 5097–5112, 2017.

[40] M. S. Kulie, R. Bennartz, T. J. Greenwald, Y. Chen, and F. Weng, "Uncertainties in microwave properties of frozen precipitation: Implications for remote sensing and data assimilation," *J. Atmos. Sci.*, vol. 67, no. 11, pp. 3471–3487, 2010.

[41] U. Löhnert, S. Kneifel, A. Battaglia, M. Hagen, L. Hirsch, and S. Crewell, "A multisensor approach toward a better understanding of snowfall microphysics: The Tosca project," *Bull. Amer. Meteorol. Soc.*, vol. 92, no. 5, pp. 613–628, 2011.

[42] Y. Wang, G. Liu, E.-K. Seo, and Y. Fu, "Liquid water in snowing clouds: Implications for satellite remote sensing of snowfall," *Atmos. Res.*, vol. 131, pp. 60–72, 2013.

[43] Y. You, G. Liu, Y. Wang, and J. Cao, "On the sensitivity of tropical rainfall measuring mission (TRMM) microwave imager channels to overland rainfall," *J. Geophys. Res., Atmos.*, vol. 116, no. D12, 2011.

[44] A. Y. Hou *et al.*, "The global precipitation measurement mission," *Bull. Amer. Meteorol. Soc.*, vol. 95, no. 5, pp. 701–722, 2014.

[45] Y. You *et al.*, "Improving cross-track scanning radiometers' precipitation retrieval over ocean by morphing," *J. Hydrometeorol.*, vol. 22, no. 9, 2393–2406, 2021.

[46] T. Kubota *et al.*, "Global precipitation map using satellite-borne microwave radiometers by the GSMaP project: Production and validation," *IEEE Trans. Geosci. Remote Sens.*, vol. 45, no. 7, pp. 2259–2275, Jul. 2007.

[47] G. J. Huffman *et al.*, "NASA global precipitation measurement (GPM) integrated multi-satellite retrievals for GPM (IMERG)," *Algorithm Theor. Basis Document Vers. 4*, vol. 26, pp. 1–39, 2015.

[48] C. Kongoli, H. Meng, J. Dong, and R. Ferraro, "A snowfall detection algorithm over land utilizing high-frequency passive microwave measurements-application to ATMS," *J. Geophys. Res., Atmos.*, vol. 120, no. 5, pp. 1918–1932, 2015.

[49] M. Goldberg, "The joint polar satellite system overview," in *Proc. IEEE Int. Geosci. Remote Sens. Symp.* 2018, pp. 1581–1584.

[50] G. L. Stephens *et al.*, "The CloudSat mission and the a-train: A new dimension of space-based observations of clouds and precipitation," *Bull. Amer. Meteorol. Soc.*, vol. 83, no. 12, pp. 1771–1790, 2002.

[51] J. Zhang *et al.*, "Multi-radar multi-sensor (MRMS) quantitative precipitation estimation: Initial operating capabilities," *Bull. Amer. Meteorol. Soc.*, vol. 97, no. 4, pp. 621–638, 2016.

[52] J. Zhang, Y. Qi, K. Howard, C. Langston, and B. Kaney, "Radar quality index (RQI)-A combined measure of beam blockage and VPR effects in a national network," *Int. Assoc. Hydrol. Sci. Publ.*, vol. 351, pp. 388–393, 2011.

[53] P. Romanov, "Global multisensor automated satellite-based snow and ice mapping system (GMASI) for cryosphere monitoring," *Remote Sens. Environ.*, vol. 196, pp. 42–55, 2017.

[54] D. A. Hastings and P. Dunbar, "Development & assessment of the global land one-km base elevation digital elevation model (GLOBE)," *GIS-Between Vis. Appl.*, vol. 4, no. 6, pp. 218–221, 1998.

[55] D. S. Wilks, *Statistical Methods in the Atmospheric Sciences*. San Francisco, CA, USA: Academic, 2011, vol. 100.

[56] E. M. Sims and G. Liu, "A parameterization of the probability of snow-rain transition," *J. Hydrometeorol.*, vol. 16, no. 4, pp. 1466–1477, 2015.

Yalei You received the B.S. and M.S. degrees in atmospheric science from Yunnan University, Kunming, Yunnan, China, in 2005 and 2008, respectively, and the Ph.D. degree in meteorology from Florida State University, Tallahassee, FL, USA, in 2013.

He is currently an Associate Research Scientist with the Earth System Science Interdisciplinary Center (ESSIC) and the Cooperative Institute for Satellite Earth System Studies (CISESS)-Maryland, University of Maryland (UMD), College Park, MD, USA. His research interests include passive microwave precipitation algorithm development, precipitation data set validation, and microwave instrument calibration.

Dr. You has served as an Associate Editor for *Journal of Hydrometeorology* and *Journal of Applied Meteorology and Climatology*.

Huan Meng received the M.S. degree in physical oceanography from Florida State University, Tallahassee, FL, USA, in 1993, and the Ph.D. degree in hydrology from Colorado State University, Fort Collins, CO, USA, in 2004.

She is currently a Physical Scientist with NOAA/NESDIS Center for Satellite Applications and Research. Her research interest is in satellite remote sensing including algorithm development, calibration and validation, and satellite product climate data record (CDR). Her current research focuses on snowfall detection and snowfall rate estimation using satellite passive microwave observations.
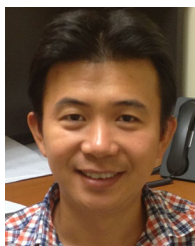
Jun Dong received the Ph.D degree in geophysical fluid dynamics from Florida State University, Tallahassee, FL, USA, in 2012.

He is currently a Faculty Specialist with Earth System Science Interdisciplinary Center (ESSIC) and Cooperative Institute for Satellite Earth System Studies (CISESS)-Marylandof, University of Maryland. He has over fifteen years of experience in methodology, physical oceanography and remote sensing. At ESSIC/CISESS, his work focuses on microwave satellite snowfall rate (SFR) retrieval algorithm development, implementation and real-time SFR product maintenance.
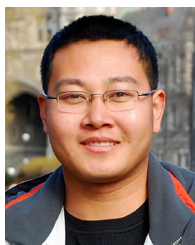
Yongzhen Fan received the B.S. degree in electronic science from Xi'an University of Science and Technology, Xi'an, China, in 2004, and the Ph.D. degree in physics from Stevens Institute of Technology, Hoboken, NJ, USA, in 2016.

He is currently an Associate Research Scientist with the Earth System Science Interdisciplinary Center (ESSIC) and the Cooperative Institute for Satellite Earth System Studies (CISESS)-Maryland, University of Maryland (UMD), College Park, MD, USA. His research interests include radiative transfer theory, machine learning, satellite remote sensing of ocean color, aerosols and snowfall.

Ralph R. Ferraro received the B.S. degree from Cook College, Rutgers University, New Brunswick, NJ, USA, and the M.S. degree from the University of Maryland, College Park, MD, USA, in 1980 and 1982, respectively, both in meteorology.

He is currently the Associate Director with the Earth System Science Interdisciplinary Center (ESSIC), University of Maryland, College Park, MD, USA. His research interest includes the development of operational hydrological cycle products from passive microwave satellite measurements, and the fusion of such measurements with other remotely sensed data.

Guojun Gu received the Ph.D. degree in meteorology and physical oceanography from Rosenstiel School of Marine and Atmospheric Science (RSMAS), University of Miami, Miami, FL, USA, in 2001.

He is currently an Associate Research Scientist with the Earth System Science Interdisciplinary Center (ESSIC), University of Maryland, College Park, MD, USA. His research interests include satellite precipitation analysis and validation, atmospheric convection and precipitation processes, and climate variability and change in precipitation and extreme events.

Likun Wang received the B.S. degree in atmospheric sciences and the M.S. degree in meteorology from Peking University, Beijing, China, in 1996 and 1999, respectively, and the Ph.D. degree in atmospheric sciences from University of Alaska Fairbanks, Fairbanks, AK, USA, in 2004.

He currently is an Associate Research Scientist with the Earth System Science Interdisciplinary Center (ESSIC) in University of Maryland (UMD), College Park, MD, USA in support of NOAA satellite sensor calibration and validation program.

Dr. Wang serves as the chair of World Meteorological Organization (WMO) sponsored Global Space-based Inter-Calibration System (GSICS) infrared sensor working group.